Ⓔ

An Automatic *P*-Phase Arrival-Time Picker

by Erol Kalkan

Abstract Presented is a new approach for picking *P*-phase arrival time in single-component acceleration or broadband velocity records without requiring detection interval or threshold settings. The algorithm $P_{PHASE}P_{ICKER}$ transforms the signal into a response domain of a single-degree-of-freedom (SDOF) oscillator with viscous damping and then tracks the rate of change of dissipated damping energy to pick *P*-wave phases. The SDOF oscillator has a short natural period and a correspondingly high resonant frequency, which is higher than most frequencies in a seismic wave. It also has a high damping ratio (60% of critical). At this damping level, the frequency response approaches the Butterworth maximally flat magnitude filter, and phase angles are preserved. The relative input energy imparted to the oscillator by the input signal is converted to elastic strain energy and then dissipated by the damping element as damping energy. The damping energy yields a smooth envelope over time; it is zero in the beginning of the signal, zero or near zero before the *P*-phase arrival, and builds up rapidly with the *P* wave. Because the damping energy function changes considerably at the onset of the *P* wave, it is used as a metric to track and pick the *P*-phase arrival time. The $P_{PHASE}P_{ICKER}$ detects *P*-phase onset using the histogram method. Its performance is compared with picking techniques using short-term-average to long-term-average ratio, and a picking method that finds the first *P*-phase arrival time using the Akaike information criterion. A large set of records with various intensities and signal-to-noise ratios is used for testing the $P_{PHASE}P_{ICKER}$, and it is demonstrated that $P_{PHASE}P_{ICKER}$ is able to more accurately pick the onset of genuine signals against the background noise and to correctly distinguish between whether the first arrival is a *P* wave (emergent or impulsive) or whether the signal is from a faulty sensor.

Online Material: MATLAB script for *P*-phase arrival time picking.

Introduction

In many seismological applications—including locating earthquakes, source mechanism analysis, and ground-motion processing—the onset time of the *P*-wave phase is needed. In semiautomatic processing, which is common to many seismic networks, the picking algorithm computes initial picks and an analyst refines them manually by inspections and corrections, because humans generally pick the *P*-wave arrival time more accurately, especially for waveforms with low signal-to-noise ratio (SNR). This manual process is subjective and time consuming. Today, handling vast amounts of triggered and continuous data from various seismic networks, in particular for earthquake early warning and automated ground-motion processing, requires efficient (less time-consuming) and equally objective alternatives.

Since the 1980s, numerous techniques have been proposed for detecting and picking arrivals of different seismic waves. These techniques look for changes in energy, polari-
zation, and frequency content or other metrics of seismic waves with respect to the background or long-term fluctuations of the corresponding metric. In these techniques, seismic waves are often filtered in advance. The filtering is needed to reduce the background noise or strengthen the signal. The seismic signal is typically strengthened within predefined (or dynamically identified) frequency bands or along certain polarization directions (Lomax *et al.*, 2012).

Among *P*-phase onset time picking techniques, the short-term-average to long-term-average ratio (STA/LTA) has been the convention since the late 1980s (Allen, 1978, 1982; Blandford, 1982; Baer and Kradolfer, 1987; Ruud and Husebye, 1992; Tarvainen, 1992; Earle and Shearer, 1994). This technique is based on comparison between an STA of a characteristic function of the signal and an LTA of this characteristic function. The absolute value or the square of the signal or its time derivative is often selected as the characteristic

function. The detection occurs when the STA/LTA ratio exceeds a predetermined or dynamically specified threshold value. This technique is well suited for detecting amplitude changes; however, its accuracy heavily depends on the detection interval and threshold settings. It also picks up pulse-like noises, especially those contained in microtremors, unrelated to the earthquake signal (Akazawa, 2004).

Autoregressive (AR) techniques are also commonly used for phase picking. These techniques are based on the assumption that the seismogram can be divided into locally stationary segments, each modeled as an AR process, and the intervals before and after the onset time are two different stationary processes with different statistical properties (Sleeman and van Eck, 1999; Rastin et al., 2013). To detect an ideal time instant that splits statistical properties of the subwindow before the onset (signal containing background noise) from those of the subwindow after the onset (signal containing seismic waves and background noise), AR techniques analyze different windows of time series. For example, typical seismic noise is well represented by a relatively low-order AR process, whereas seismic signals are usually represented by a higher-order AR process (Leonard and Kennett, 1999). The Akaike information criterion (AIC) helps to determine the order of the AR process when fitting a time series with an AR process, which indicates the model misfit as well as the unreliability (Akaike, 1974). This method has been used in onset estimation by analyzing the variation in AR coefficients representing both multicomponent and single-component traces of broadband and short-period seismograms (Takanami and Kitagawa, 1988; Leonard and Kennett, 1999). When the order of the AR process is fixed, the AIC function is a measure for the model fit. The point where the AIC is minimized determines the optimal separation of the two stationary time series in the least-squares sense and thus is interpreted as the phase onset (Sleeman and van Eck, 1999); this picker is known as AR–AIC picker (Leonard, 2000). In contrast, Maeda (1985) calculates the nonparametric AIC function directly from the seismogram without using the AR coefficients. If there are multiple seismic phases in a time window, the AIC picker will choose the stronger phase. On the other hand, the AIC picker will usually pick an onset for any segment of data, no matter whether there is a true phase arrival in the time window or not. Using the segment of the waveform from beginning to the absolute peak value improves the performance of the AIC picker. The AIC picker can neither distinguish nonearthquake signals without P phase (e.g., vibration noise in urban areas) nor identify signals from a faulty sensor (the signals from faulty sensors are often contaminated by mechanical and/or digital noise; Jones et al., 2016).

Artificial neural networks (e.g., Dai and MacBeth, 1995; Mousset et al., 1996; Wang and Teng, 1997; Zhao and Takano, 1999; Gentili and Michelini, 2006), wavelet transforms (e.g., Anant and Dowla, 1997; Zhang et al., 2003; Hafez et al., 2010), analysis of wave polarization (Cichowicz, 1993), pattern recognition (Joswig, 1990), hybrid techniques (such as the combination of energy analysis, differences in instantaneous frequency, and an AR representation of the seismic record; e.g., Bai and Kennett, 2000; Akazawa, 2004), cross correlation of the running-window energy ratios of the STA/LTA of seismic data (Forghani-Arani et al., 2013), and use of higher-order statistics based on skewness and kurtosis (Saragiotis et al., 2002; Kuperkoch et al., 2010; Baillard et al., 2014; Ross and Ben-Zion, 2014) are among other methods proposed to detect P-wave phases. A common disadvantage of these methods is that they require one or more of the following as a priori: detection interval, threshold settings, an approximate knowledge of the moveout character for an event, and tuning of picking parameters specific to intensity and/or frequency content of the signal.

Presented here is a new algorithm for picking the P-phase arrival time in single-component ground-motion acceleration or broadband velocity records without requiring a detection interval or threshold settings. This algorithm, called $P_{PHASE}P_{ICKER}$, transforms the signal into a response domain of a linear-elastic fixed-base single-degree-of-freedom (SDOF) oscillator with viscous damping, and then tracks the rate of change (power) of dissipated damping energy to pick the P-wave phase. To prevent resonance, the SDOF oscillator has a short natural period ($T_n = 0.01$ s) and a correspondingly high resonant frequency, which is higher than most frequencies in a seismic wave. It also has a high damping ratio ($\zeta = 0.6$) similar to short-period seismometers, typically used to study body waves. At 60% or higher damping ratio, the frequency response approaches the Butterworth maximally flat magnitude filter, and phase angles are preserved. This means that the frequency content of the input signal is carried to the relative response of the oscillator for P-phase picking, an important consideration for selecting $T_n = 0.01$ s and $\zeta = 0.6$.

The input energy imparted to the SDOF oscillator by the seismic signal (base excitation) is converted to elastic strain energy and then dissipated by the damping element as damping energy. The damping energy yields a smooth dissipation envelope over time. It is zero in the beginning of the signal, zero or near zero before the P-phase arrival, and builds up rapidly following the P phase. Because the damping energy function changes considerably at the onset of the signal, it can be used as a convenient metric to track and detect the P-phase arrival time even in signals with low SNR. $P_{PHASE}P_{ICKER}$ detects the P-phase onset in only milliseconds of the computer's central processing unit time. Its performance is compared with the conventional picking techniques based on (1) STA/LTA (Allen, 1982), (2) the picking method of Maeda (1985), which finds first P-phase arrival using the AIC, and (3) manual picking results. In the following, the theoretical background of $P_{PHASE}P_{ICKER}$ is explained first with examples using six teleseismic records and two three-component strong-motion acceleration records. Its systematic evaluation is presented at the end, based on 1652 acceleration and velocity waveforms with various intensities and SNRs from the 2014 moment magnitude (**M**) 6.0 South Napa, California, earthquake and its

Table 1
Abbreviations and Symbols Present in This Article

Abbreviation or Symbol	Definition
c	Damping term of single-degree-of-freedom (SDOF) oscillator
E_I	Absolute (total) input energy
E_I'	Relative input energy
E_K	Absolute (total) kinetic energy
E_K'	Relative kinetic energy
E_S	Elastic strain energy
E_ζ	Damping energy
i	Histogram bin number
i_{low}	Lowest-indexed histogram bin
i_{high}	Highest-indexed histogram bin
k	Stiffness term of SDOF oscillator
m	Mass of SDOF oscillator
M	Moment magnitude
M	Number of histogram bins
t	Time instant
T_D	Natural period of damped vibration of SDOF oscillator
T_n	Natural period of undamped vibration of SDOF oscillator
u	Relative displacement of mass of SDOF oscillator with respect to base
u_g	Ground displacement
u_t	Absolute (total) displacement of mass of SDOF oscillator
$\dot{u}$	Relative velocity of mass of SDOF oscillator with respect to base
$\dot{u}_g$	Ground velocity
$\ddot{u}_g$	Ground acceleration
$\ddot{u}_t$	Absolute (total) acceleration of mass of SDOF oscillator
y	Seismic signal (either ground acceleration or ground velocity)
y_{max}	Maximum amplitude value of power of damping energy, y
y_{min}	Minimum amplitude value of power of damping energy, y
y_R	Range of power of damping energy
Δy	Histogram bin width
Δt	Sample interval
ζ	Damping ratio
ω_D	Cyclic frequency

M 3.6 aftershock. The list of abbreviations and symbols used throughout this article is given in Table 1.

Energy Formulation of Single-Degree-of-Freedom Oscillator

Figure 1 shows two types of SDOF oscillators with viscous (velocity dependent) damping idealized as moving and fixed base. For both oscillators, the equation of motion, a second-order ordinary differential equation, is

$$m\ddot{u}_t + c\dot{u} + ku = 0, \tag{1}$$

in which m is the mass, c is the damping term, and k is the stiffness term. u_t ($u_t = u + u_g$) is the absolute (total) dis-
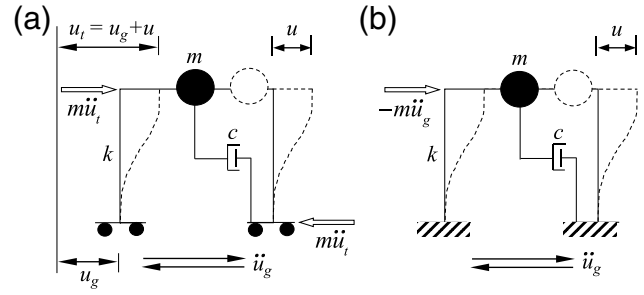

Figure 1. Mathematical models of idealized single-degree-of-freedom (SDOF) oscillators with viscous damping for (a) absolute energy formulation (moving base) and (b) relative energy formulation (fixed base).

placement of the mass, u_g is the ground displacement, and u is the relative displacement of the mass with respect to base (i.e., ground). Equation (1) can be rewritten as

$$m\ddot{u} + c\dot{u} + ku = -m\ddot{u}_g. \tag{2}$$

The right side of equation (2) is the excitation function associated with the ground acceleration ($\ddot{u}_g$). Integrating equations (1) and (2) with respect to u leads to two different definitions of seismic input energy. Integrating equation (1) with respect to u gives the absolute (total) energy formulation of a linear-elastic viscous-damped SDOF oscillator with moving base (Fig. 1a), subjected to base motion ($\ddot{u}_g$) as follows:

$$\frac{m[\dot{u}_g + \dot{u}]^2}{2} + \int c\dot{u}\,du + \int ku\,du = \int m[\ddot{u}_g + \ddot{u}]du_g. \tag{3}$$

For convenience, the right side of equation (3) can be rewritten as

$$\int m[\ddot{u}_g + \ddot{u}]du_g = \int_0^t m[\ddot{u}_g + \ddot{u}]\dot{u}_g dt, \tag{4}$$

in which t denotes time. Equation (3) can also be expressed in a general form, which identifies the different energy components as

$$E_K + E_\zeta + E_S = E_I, \tag{5}$$

in which E_K is the absolute-kinetic energy, E_ζ is the damping energy, and E_S is the elastic strain energy. The sum of these terms is equal to energy imparted to the SDOF oscillator, which is the absolute-input energy (E_I).

As a corollary, integration of equation (2) with respect to relative displacement of mass (u) results in relative energy formulation of a linear-elastic viscous damped fixed-based SDOF oscillator, shown in Figure 1b as

$$\frac{m\dot{u}^2}{2} + \int c\dot{u}\,du + \int ku\,du = -\int m\ddot{u}_g\,du$$
$$= -\int_0^t m\ddot{u}_g\dot{u}\,dt. \tag{6}$$

Equation (6) can be expressed in terms of the following energy components:

$$E_K' + E_\zeta + E_S = E_I', \tag{7}$$

in which E_K' is the relative-kinetic energy and E_I' is the relative-input energy. E_I in equation (5) represents the work done by the inertia force ($m\ddot{u}_t$) acting on the mass, which is equivalent to the work done by the total base-shear force on the ground displacement. On the other hand, E_I' in equation (7) represents the work done on a fixed-base oscillator by an equivalent-lateral force, thereby excluding rigid body translation effects. The difference between the two energy formulations (i.e., E_I' vs. E_I) is a result of the different definitions of kinetic energy (E_K' vs. E_K), whereas damping (E_ζ) and strain energy (E_S) terms remain identical in both definitions. In a viscously damped SDOF oscillator, the rate of change (power) of damping energy dissipated for a unit mass is computed by differentiating E_ζ with respect to time (t) as

$$\frac{dE_\zeta}{dt} = 2\zeta\omega_D \dot{u}^2, \tag{8}$$

in which ω_D is the cyclic frequency, defined as $2\pi/T_D$. T_D is the natural period of damped vibration related to the natural period of vibration without damping (T_n) by

$$T_D = T_n/\sqrt{1 - \zeta^2}. \tag{9}$$

The $P_{PHASE}P_{ICKER}$ Algorithm

$P_{PHASE}P_{ICKER}$ operates on a digital time-series signal with sample interval Δt. This signal may be either an acceleration record ($\ddot{u}_g$) or a broadband velocity record ($\dot{u}_g$) as output from the recorder without filtering or baseline correction. The $P_{PHASE}P_{ICKER}$ finds the onset of the P phase by tracking the power of the damping energy. This energy term is formulated in a linear-elastic response domain of a fixed-base SDOF oscillator with viscous damping, as shown in Figure 1b. To eliminate resonance, the SDOF oscillator with unit mass has a short natural period (damped natural period $T_D = 0.0115$ s, very close to the undamped natural period $T_n = 0.01$ s) and a correspondingly high resonant frequency, which is higher than most frequencies in a seismic wave. The damping ratio is selected as $\zeta = 0.6$ (60% of critical damping) to be similar to short-period seismometers, which are typically used to study body waves. At this damping level, the frequency response approaches the Butterworth maximally flat magnitude filter, and phase angles are preserved in the response of the oscillator. With these specific frequency and damping attributes, the SDOF oscillator returns to the equilibrium position quickly without free vibration and without contaminating the energy characteristics of the SDOF response associated with the input motion.

Under seismic excitation, the input energy imparted to the oscillator through the ground excitation is converted to elastic response and dissipated by the damping element. Thus, the relative motion of the mass (u), and hence relative-kinetic energy of the SDOF oscillator, becomes negligibly small. To demonstrate the effects of T_n and ζ on energy parameters in equation (7), two SDOF oscillators are used as examples. The first oscillator has a short period and high damping ratio ($T_n = 0.01$ s, $\zeta = 0.6$) as in $P_{PHASE}P_{ICKER}$. The second oscillator has a long period and low damping ratio ($T_n = 1$ s, $\zeta = 0.1$) selected as an end case. These SDOF oscillators are subjected to a raw acceleration record, shown in Figure 2a, and the resultant energy parameters are computed by equation (6). These parameters are plotted side-by-side in Figure 2b–e. For the short-period oscillator, relative-input energy (which is the summation of relative-kinetic energy, elastic strain energy, and damping energy) is mostly stored and released as strain energy and then dissipated by viscous damping. The kinetic energy of the oscillator is negligibly small because the mass barely moves with respect to the base due to the short vibration period and high damping ratio. For the long-period oscillator with much lower damping ratio, however, most of the input energy is converted to kinetic energy due to the moving mass and then dissipated by a damping element as damping energy. For both oscillators, relative energy equals damping energy at the end of the motion. Because the damping energy is a cumulative parameter, proportional to square of the relative velocity of the mass (see equation 8), it results in a smooth-envelope function over time as shown in Figure 2e. It is zero in the beginning of the record, near zero (or flat) before the P-phase arrival, and builds up immediately following the P phase. The damping energy function, hence its power, changes considerably at the onset of the signal because background noise and signal typically have different frequency distributions. Unlike the long-period oscillator, the oscillator with a short vibration period is more sensitive to this change (see Fig. 2e). The long-period oscillator yields delayed and out-of-phase response. $P_{PHASE}P_{ICKER}$ makes use of the smoothness attribute of the damping energy to detect the P-wave phase arrival time. Note that it is more difficult to detect P-phase onset in a jagged-time series. For that reason, the input energy is not used for detection because it is unsmooth due to the contribution of kinetic energy as shown in Figure 2b.

How $P_{PHASE}P_{ICKER}$ works is explained in detail on a broadband P-wave record in Figure 3. This low-SNR record, which is the same record in figure 4 of Lomax et al. (2012), is a good example, because it has a clear and longer-period P onset for a small local event. For detecting the P-phase onset, Lomax et al. used a modified STA/LTA method, which is based on the work by Baer and Kradolfer (1987) and Allen (1978, 1982). Their picking results are repeated here for comparison.

To conduct a broadband picking, the first step is to detrend and filter the raw signal to reduce the noise level. For this purpose, an acausal (zero-shift) fourth-order band-pass Butterworth filter is used. The filtered record is detrended by removing the best straight-line linear trend from the data. Next, a fixed-base SDOF oscillator with a unit mass is
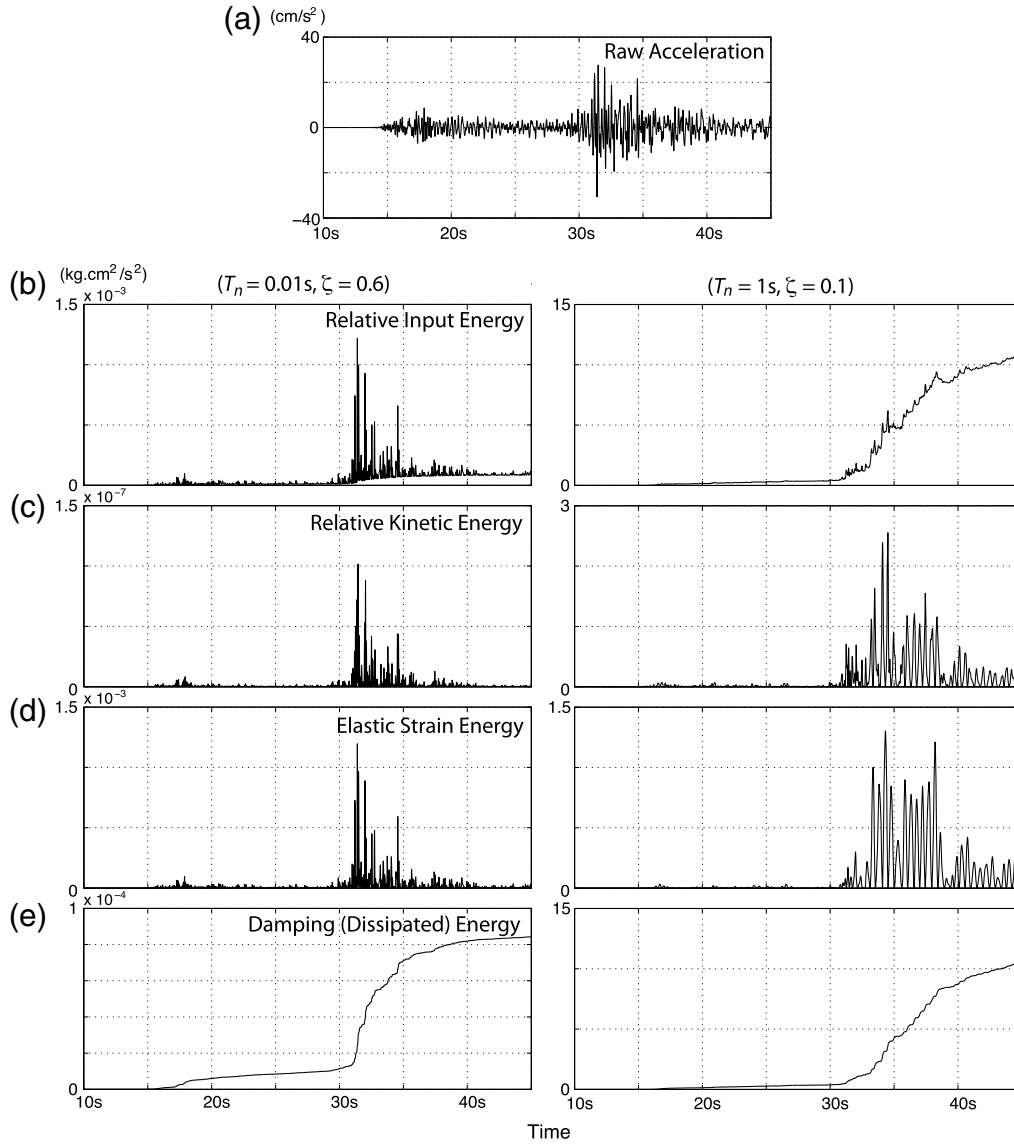
Figure 2.   Raw acceleration record of AZ-BZN station with 100 samples/s from the 29 March 2014 **M** 5.1 (**M**, moment magnitude) La Habra earthquake in southern California is used to demonstrate the energy metrics for two SDOF oscillators idealized as a fixed base with a short period and high damping ratio ($T_n = 0.01$ s, $\zeta = 0.6$) and with a long period and low damping ratio ($T_n = 1$ s, $\zeta = 0.1$). Traces show the following: (a) raw acceleration signal; (b) relative-input energy imparted to the SDOF oscillator; (c) relative-kinetic energy of the moving mass with respect to base; (d) elastic strain energy; and (e) energy dissipated by viscous damping. Energy is in unit of kg·cm/s^2. Note the smoothness of damping energy in (e).

constructed with $T_n = 0.01$ s and $\zeta = 0.6$. Equation (2) is solved in the time domain to compute the relative velocity ($\dot{u}$) of the mass. Once $\dot{u}$ is known, equation (6) can be used to compute the different energy metrics. Figure 3b–e illustrates the relative input energy, relative kinetic energy, elastic strain energy, and damping energy time histories, respectively. The power of damping (dissipated) energy is plotted in Figure 3f, following equation (8). The next step is to pick the onset time of *P*-wave in Figure 3f. As a picking algorithm, the histogram method (Solomon *et al.*, 2001; Institute of Electrical and Electronics Engineers [IEEE], 2003) is used. Although one may use another method, for instance the AIC method, the histogram method was preferred because it does not re-

quire any detection interval or threshold settings. To generate a histogram, the amplitude range is divided into *M* equal-amplitude intervals. The amplitude interval is called the histogram bin width, and *M* is the number of bins or the histogram size. The histogram is formed by counting the number of times a time-series value fits within a particular histogram bin; this is referred to as the bin count.

The algorithm is described step-by-step in the following:

1. Determine the maximum and minimum amplitudes, y_{max} and y_{min}, of the power of damping energy (see Fig. 3f), which will correspond to lower and upper state levels.
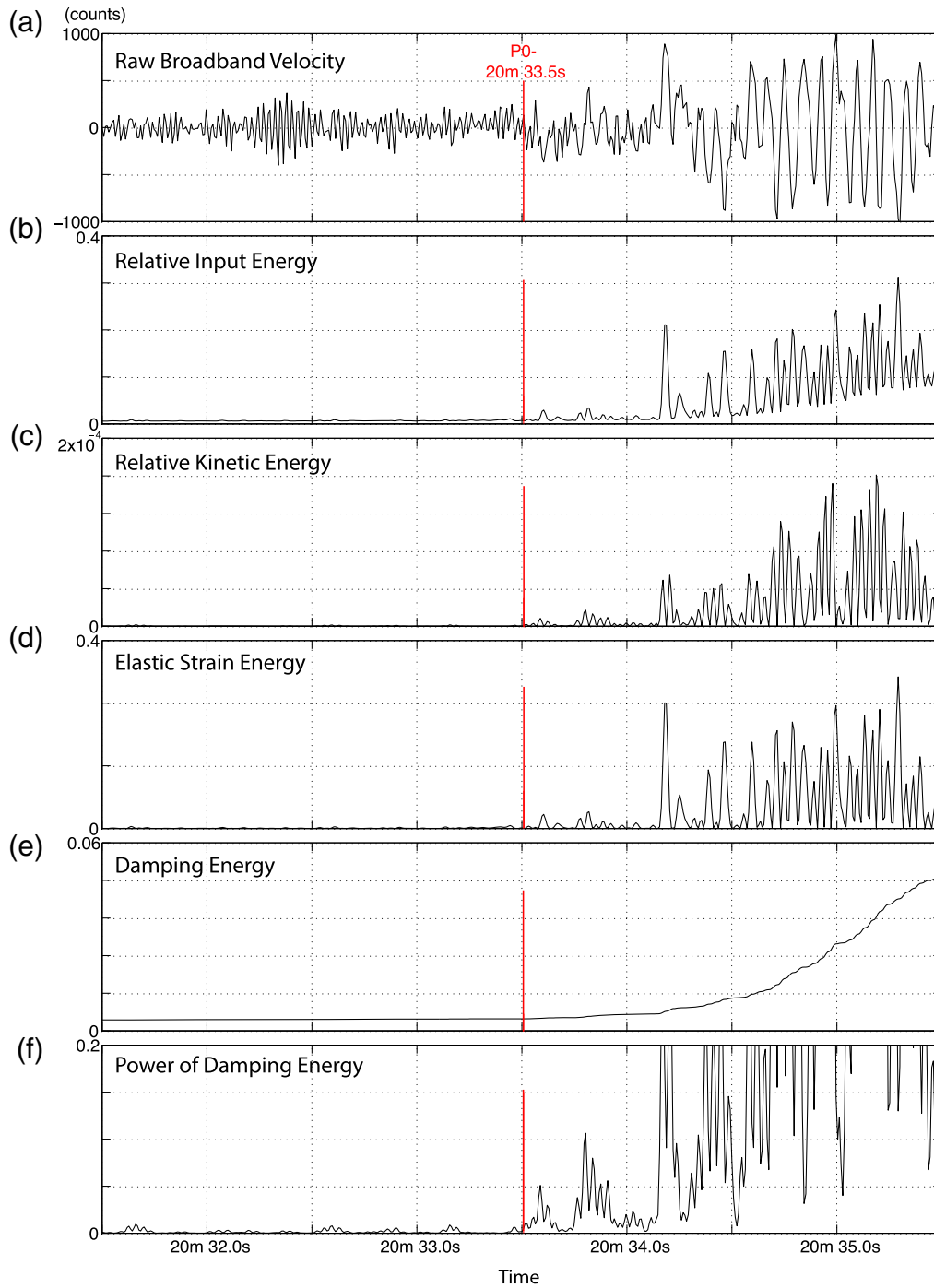2. Calculate the amplitude range y_R of the power of damping energy using $y_R = y_{max} - y_{min}$.

Figure 3. Noisy signal example of broadband velocity record and the *P*-wave first-arrival detection result for a small regional event recorded in 19 September 2010 at ISNet station in Italy with 125 samples/s. Traces are as follows: (a) raw broadband velocity; (b) relative-input energy imparted to the SDOF oscillator; (c) relative-kinetic energy due to moving mass with respect to base; (d) elastic strain energy; (e) energy dissipated by damping element; and (f) power of damping energy. Traces (b)–(f) are based on a fourth-pole band-pass Butterworth-filtered input signal with corner frequencies: high cut = 20 Hz and low cut = 0.1 Hz. Note the low signal-to-noise ratio (SNR) level. The emergent *P* first arrival (*P*0−), marked by a vertical line, matches with the manual pick. Energy is shown in kg·count/s^2). The color version of this figure is available only in the electronic edition.

3. For the specified number of histogram bins (M), determine the bin width Δy as the ratio of the amplitude range to the number of bins; Δy is found by dividing y_R by M.
4. Sort the data values into the histogram bins.

5. Identify the lowest-indexed histogram bin (i_{low}) and highest-indexed histogram bin (i_{high}) with nonzero counts.
6. Divide the histogram into two subhistograms. The indexes of the lower histogram bins are $i_{low} \leq i \leq \frac{1}{2} \times (i_{high} - i_{low})$,

and the indexes of the upper histogram bins are $i_{low} + \frac{1}{2} \times (i_{high} - i_{low}) \le i \le i_{high}$.

7. The low-state level, which is the mode of the largest bin within the lower histogram, corresponds to the *P*-wave phase, and its onset is determined as the last zero crossing on the filtered seismogram before the *P*-wave phase arrival.

Although $M = 200$ is found to be sufficient for a typical seismogram by testing a large number of weak- and strong-motion records with different amplitudes and SNR values, regional or teleseismic records might need different values of bin size for good picking results.

To pick the first *P*-wave arrival, the raw signal in Figure 3a is band-pass filtered with corner frequencies 20 and 0.1 Hz, a typical frequency band used for processing seismograms. To enhance the detection, a narrower frequency band may be required if the signals have low SNRs, for example, those from microseismic events (as will be shown later). $P_{PHASE}P_{ICKER}$ picks the impulsive first arrival (*P*) at 20 min 33.5 s (marked by a vertical solid line in Fig. 3), where there is a decisive change in the energy content between the noise and signal. This change can be noticed easily on the energy plots in Figure 3b–d, and it is even more visible on the power plot in Figure 3f. The sudden change in the energy parameters occurs because the *P* wave has distinctive higher long-period energy content than the background noise even though its amplitude is similar to the noise level, thus it might not be identified by manual picking; further filtering may be necessary to emphasize the *P*-wave onset.

Similarly, the picker recovers the longer-period secondary arrival (*P*1) at 20 min 34.2 s when the raw signal is processed with low-pass corner frequency of 10 Hz, revealing more long-period content. The resulting energy plots are shown in Figure 4, where the change in energy parameters associated with the secondary arrival is apparent in Figure 4b–e, and it is even more pronounced in Figure 4f. For this particular record, the first (*P*) and second (*P*1) arrivals picked by the $P_{PHASE}P_{ICKER}$ match those reported in Lomax *et al.* (2012).

In the next example, six vertical component broadband velocity records from a small regional event with **M** 1.1 at ~2.4 km depth that occurred in Decatur, Illinois, on 16 September 2013 are used for testing. To pick the first *P*-wave arrival, the raw signals shown in Figure 5 are band-pass filtered with corner frequencies 10 and 0.5 Hz and then de-trended. The narrow passband is needed due to the presence of low- and high-frequency noise. The detection results of $P_{PHASE}P_{ICKER}$ are marked as vertical solid lines. The manual picks by a U.S. Geological Survey (USGS) analyst for the six seismograms (DEC05 through DEC12) are 12.14, 11.81, 11.63, 11.60, 11.96, and 11.79 s, respectively. The difference between the detection results of $P_{PHASE}P_{ICKER}$ and manual picks are 0, 0.04, 0.04, 0.03, −0.03, and 0 s, respectively. Such small differences demonstrate an excellent performance of $P_{PHASE}P_{ICKER}$ for detecting the onset times of *P* waves in noisy and low-amplitude signals from the microseismic event.

$P_{PHASE}P_{ICKER}$ is next applied to a three-component raw acceleration record in Figure 6. This record was obtained from an **M** 6.1 earthquake that occurred on 5 May 2014 in Thailand. This record is chosen because its HN1 component is much noisier than the other two components. $P_{PHASE}P_{ICKER}$ picks the *P*-phase onset at 61.55, 61.08, and 61.80 s, respectively, for the HN1, HN2, and UP components (marked by vertical solid lines), where there is a noticeable change in the energy content at the onset of the signal. To facilitate comparisons, the damping energy and its power are normalized in each panel by their corresponding peak values. The AIC picker of Maeda (1985) is also used for comparison; the AIC picker detects the *P*-phase onset at 60.57, 59.66, and 59.89 s for the HN1, HN2, and UP components, respectively. The manual picks (conducted by E. Kalkan) are 60.65, 61.00, and 61.70 s consistent with the $P_{PHASE}P_{ICKER}$. The maximum discrepancy between the manual picks and $P_{PHASE}P_{ICKER}$ is 0.09 s, whereas that for the AIC picker is 1.91 s.

Automatic picking of *S*-wave arrivals is challenging due to contamination of the direct *S*-wave arrival by the *P* coda and converted phases (Ross and Ben-Zion, 2014). The examples in Figure 6 show that there is a clear jump in damping energy with the *S*-wave arrival because the *S* wave contains significantly more energy than does the *P* wave. For example, in Figure 6, a clear, sharp jump around 1 min 20 s is associated with the *S*-wave arrival (vertical dashed line). $P_{PHASE}P_{ICKER}$ can be used for tracking the largest jump in damping energy associated with the *S* wave; this is, however, left for future development.

In the third example, a three-component acceleration record obtained at the NC-HMOB station of the Northern California Seismic Network during the 24 August 2014 **M** 6.0 South Napa earthquake is used for further testing $P_{PHASE}P_{ICKER}$. Figure 7 shows the HN1, HN2, and UP components. This record is selected because its vertical component is from a faulty sensor and contains noise only. For an automated processing and dissemination of ground-motion records, it is essential to identify signals from faulty sensors. The AIC picker is used again for comparison. The picking results are marked on the plots. For horizontal components, $P_{PHASE}P_{ICKER}$ yields almost the exact same picking results as the AIC picker and returns null picking for the vertical component. The reason for null picking is that the damping energy has a near constant slope due to wide-spectrum noise associated with the faulty sensor. For this reason, the histogram method computes a similar mode value for the bins and returns null picking. On the other hand, the AIC picker yields a false picking for the vertical component. This picker will usually pick an onset for any segment of data, no matter whether there is a true phase arrival in the time window or not (Jones *et al.*, 2016). As a result, the AIC picker can neither distinguish non-earthquake signals without *P* phase (e.g., vibration noise in urban areas) nor identify signals from a faulty sensor (the signals from faulty sensors are often contaminated by mechanical and/or digital noise). It should be also noted that neither
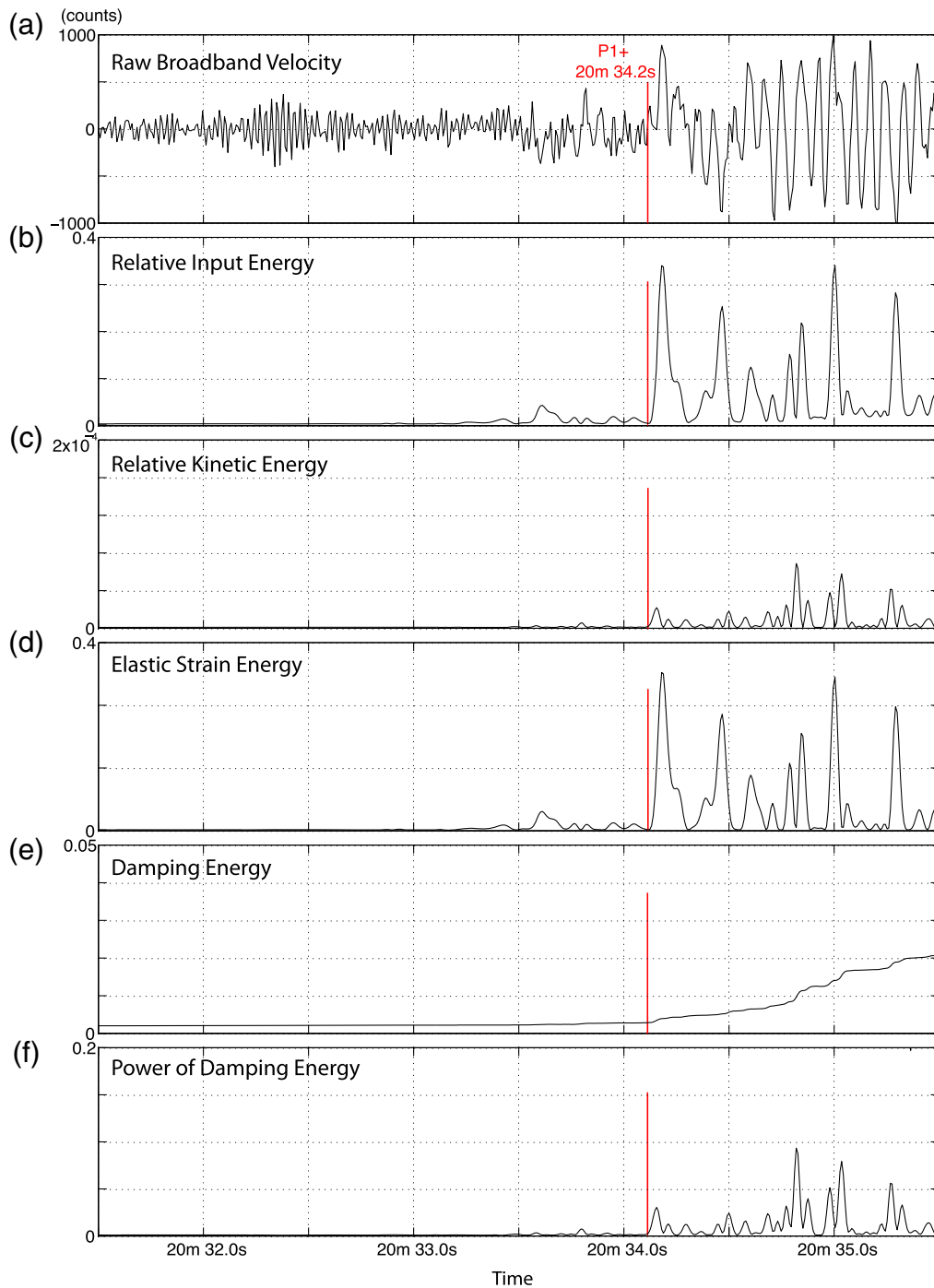
Figure 4. Emergent secondary *P* arrival (*P*1+) is shown by a vertical line for the same record as in Figure 3. Traces (b)–(f) are based on a fourth-pole band-pass Butterworth-filtered input signal with corner frequencies: high cut = 10 Hz and low cut = 0.1 Hz. The emergent secondary *P* arrival (*P*1+), marked by vertical line, matches with the manual pick. Energy is shown in kg·count/s². The color version of this figure is available only in the electronic edition.

$P_{PHASE}P_{ICKER}$ nor AIC works properly if data have glitches or dropouts.

The above examination demonstrates the accuracy of the $P_{PHASE}P_{ICKER}$ in determining the *P*-phase onsets in a few selected representative examples of acceleration and broadband velocity records. Its systematic evaluation using a large set of acceleration and broadband velocity records is presented next.

Systematic Tests on South Napa Earthquake Mainshock and Aftershock Data

The quantitative performance of $P_{PHASE}P_{ICKER}$ is compared to that of the standard STA/LTA and AIC pickers and to manual picking results using broadband velocity and strong-motion acceleration data obtained from the 2014 **M** 6.0
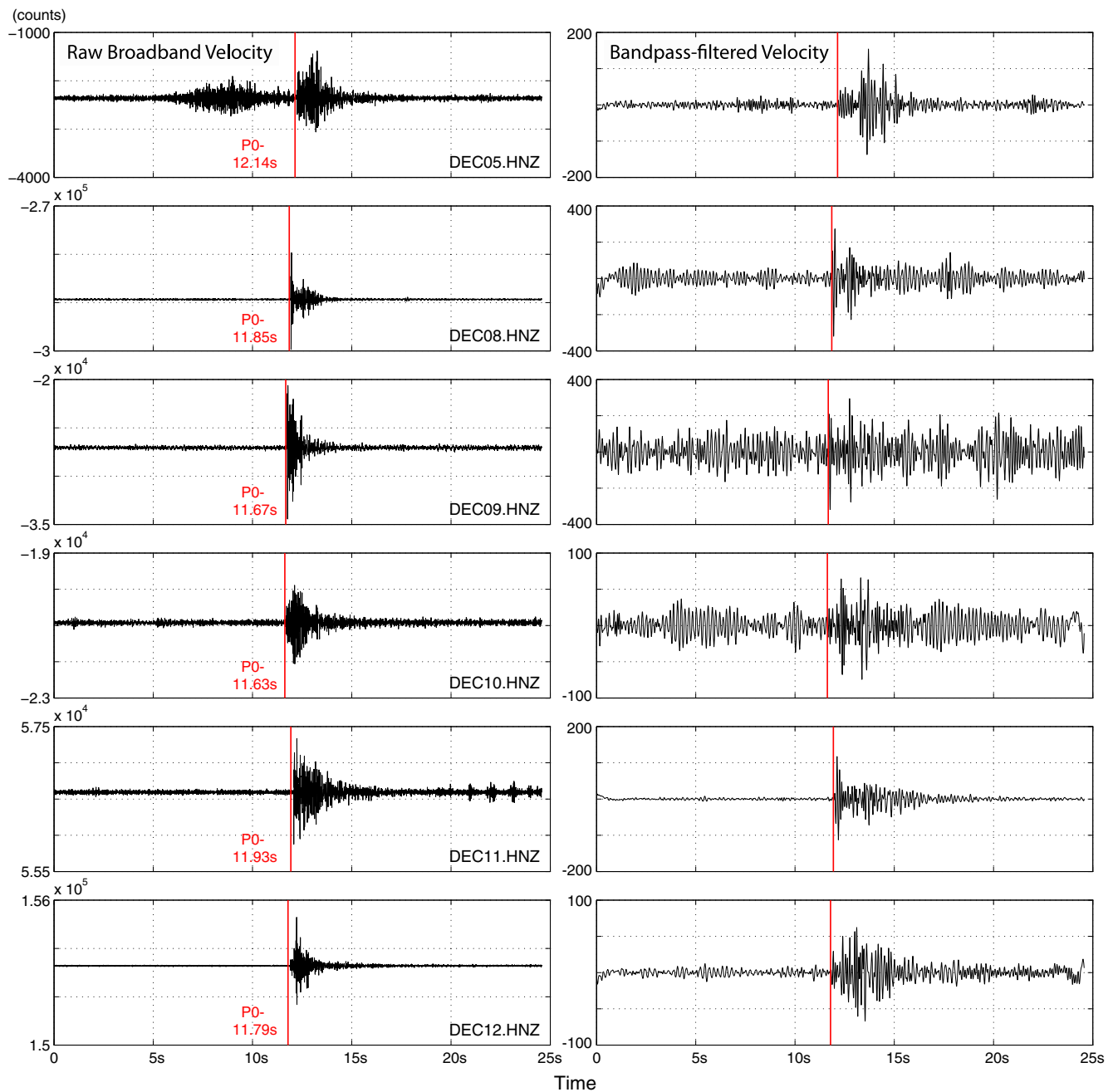
Figure 5. *P*-wave onset time detection results of $P_{PHASE}P_{ICKER}$ for vertical-component broadband velocity records obtained from a small regional event with **M** 1.1 on 16 September 2013 in Decatur, Illinois. Signals were recorded by six U.S. Geological Survey stations with 200 samples/s: (left) raw signals, and (right) fourth-pole band-pass Butterworth-filtered signals with corner frequencies: high cut = 10 Hz and low cut = 0.5 Hz. The emergent *P*-phase onset (*P*0−) detected by $P_{PHASE}P_{ICKER}$ is shown by vertical lines. Manual picks are 12.14, 11.81, 11.63, 11.60, 11.96, and 11.79 s for stations DEC05–DEC12, respectively. The color version of this figure is available only in the electronic edition.

South Napa earthquake and one of its aftershock with **M** 3.6, which occurred within three hours of the mainshock. Table 2 lists relevant information about these two events including epicenter location, magnitude, and depth.

To improve picking performance, part of the seismogram from beginning to its absolute peak is used for the AIC picker instead of the whole seismogram; this picker does not require any picking parameter. For the STA/LTA picker, the short- and long-term averaging window lengths are taken

as 1 and 8 s of the waveform, respectively. The values of the STA/LTA ratio that trigger on and trigger off are set as 2 and 1.5, respectively.

Also, it is more difficult to detect seismic onsets in waveforms with high noise content or low SNRs. Following Hildyard *et al.* (2008), the SNR is the ratio between the mean values of the amplitude squared taken in a 1 s window before and after the onset time from the manual pick. The SNR was calculated for *P*-wave arrivals from the unfiltered time series.
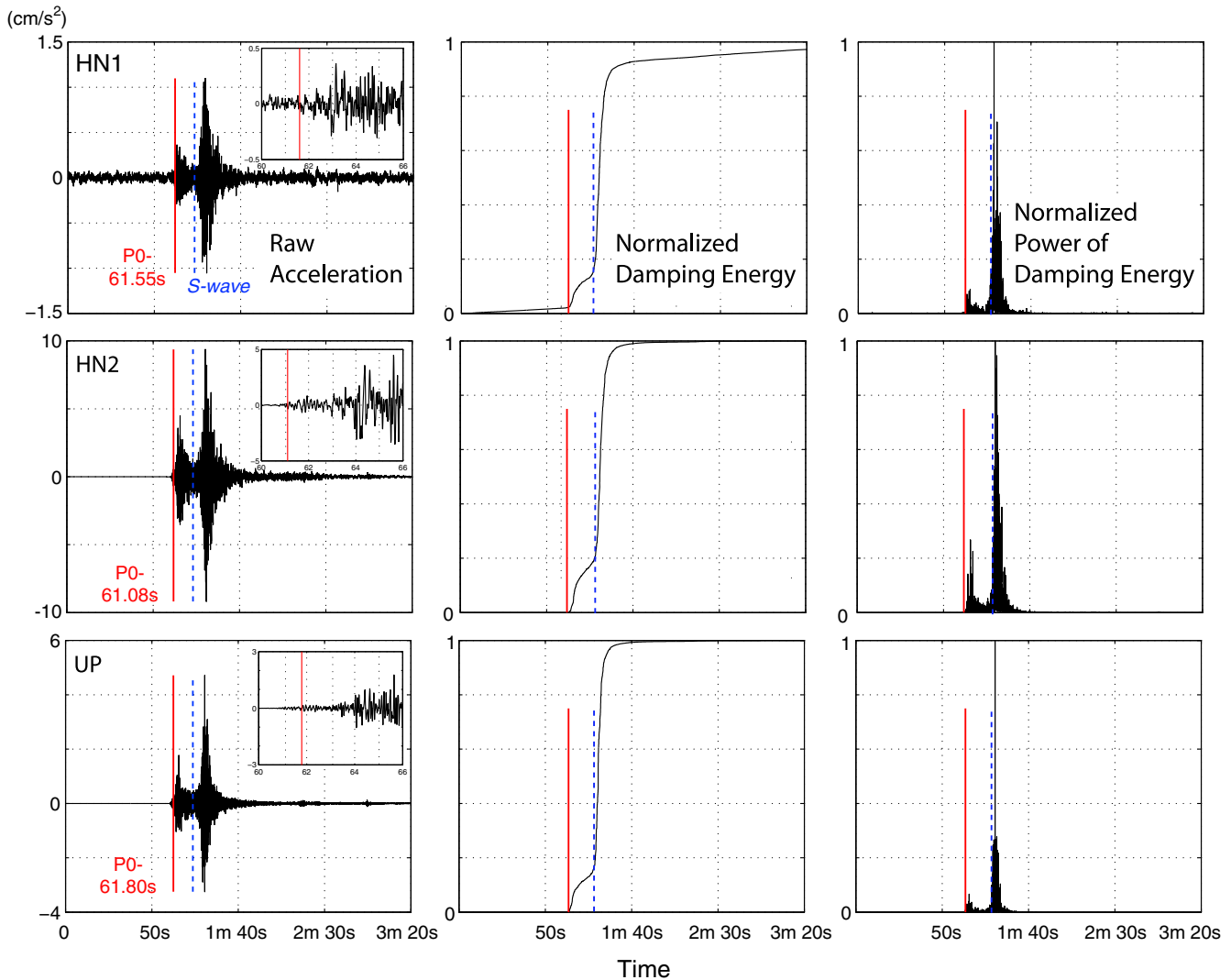
Figure 6.   *P*-phase onset time detection results of $P_{PHASE}P_{ICKER}$ for three-component acceleration record obtained from an **M** 6.1 earthquake on 5 May 2014 in Thailand with 100 samples/s: (left) raw acceleration components; (middle) normalized damping energy; (right) normalized power of damping energy. Note that the HN1 component is much noisier than the other two components. Damping energy and power plots, normalized by their associated peak values, correspond to a band-pass-filtered input signal with corner frequencies: high cut = 20 Hz and low cut = 0.1 Hz. The emergent *P*-wave onset is shown by vertical solid lines and also is repeated in close-up views in the left panels. Manual pick times are 60.65, 61.00, and 61.70 s, consistent with the $P_{PHASE}P_{ICKER}$. Vertical dashed lines demonstrate *S*-wave arrival (picked manually). The color version of this figure is available only in the electronic edition.

The mainshock strong-motion data set contains 740 acceleration waveforms with a mean SNR of 71.29 and a minimum SNR of 0.61, the mainshock broadband velocity data set has 518 waveforms with a mean SNR of 69.97 and a minimum SNR of 0.41, and the aftershock broadband velocity data set has 394 waveforms with a mean SNR of 40.82 and a minimum SNR of 0.19.

Figure 8a maps the epicenter of the mainshock and locations of strong-motion stations within 9.6–306.2 km epicentral distance. For the strong-motion data set, the time differences between the automatic and manual picks are analyzed to evaluate the accuracy of the automatic pickers. The author conducted the manual picking of *P*-phase onset times for this set. For $P_{PHASE}P_{ICKER}$, the median difference between the automatic and manual picks is -0.01 ± 0.41 s

(variance = 0.16 s^2) (Fig. 8b). For the AIC picker, this difference is 0.09 ± 0.80 s (variance = 0.64 s^2) (Fig. 8c), whereas for the STA/LTA picker the difference becomes -0.17 ± 0.77 s (variance = 0.59 s^2) (Fig. 8d). The small median and variance distribution of time differences indicate that there is little or no systematic shift with respect to manual picks. The systematic offset is much larger, especially with the STA/LTA picker, than with $P_{PHASE}P_{ICKER}$. The $P_{PHASE}P_{ICKER}$ results are much closer to manual picks as compared to those from the other two pickers. For example, 65% of the compared *P*-phase picks made by $P_{PHASE}P_{ICKER}$ are less than 0.2 s from the manual picks, compared with 57% using the AIC method and only 36% using the STA/LTA method. The distribution of STA/LTA picks shows a trend to negative residuals, indicating that
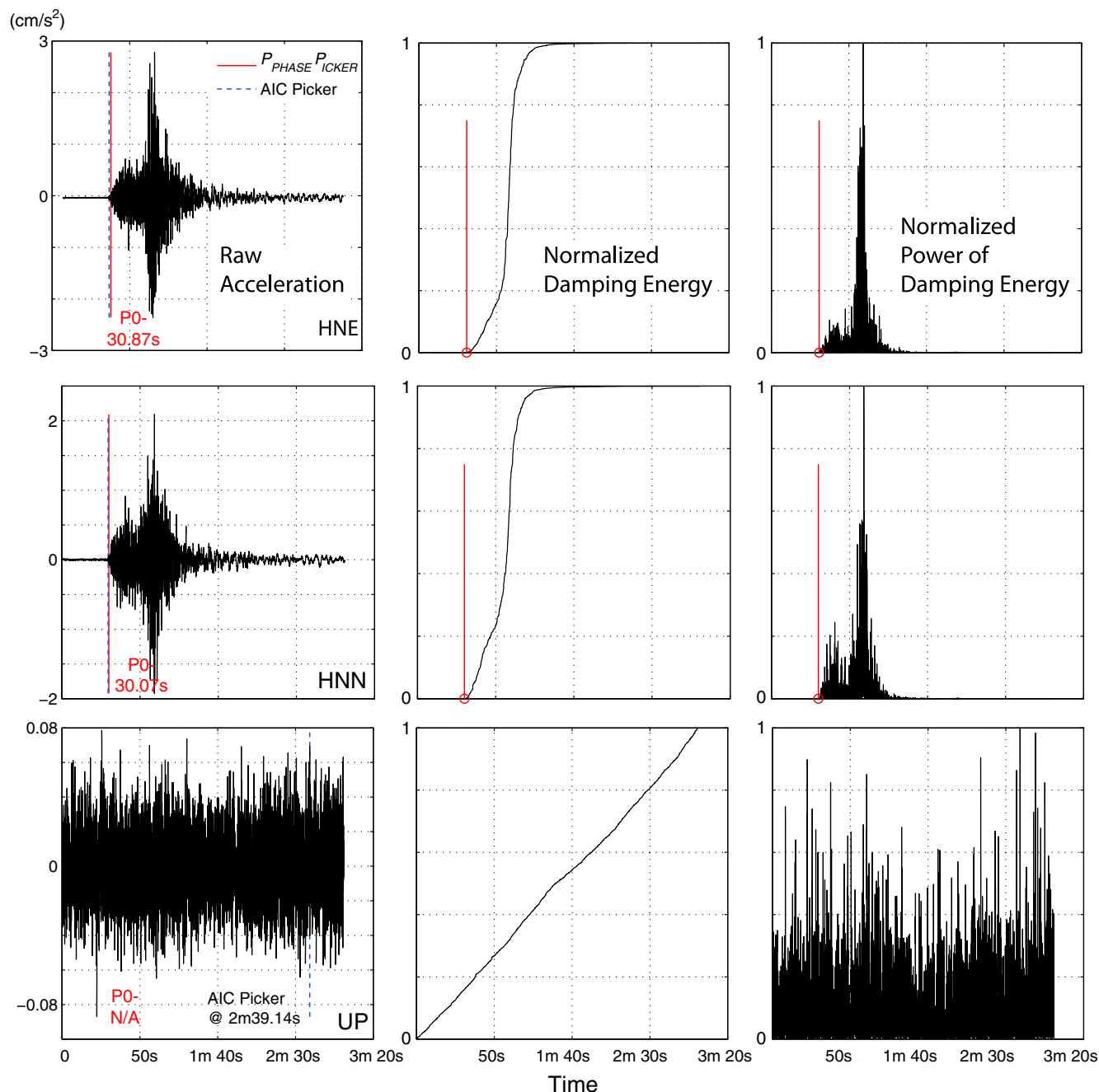
Figure 7. *P*-phase onset time detection results for three-component acceleration record obtained from the 24 August 2014 **M** 6.0 South Napa earthquake in northern California with 200 samples/s: (left) raw acceleration components; (middle) normalized damping energy; and (right) normalized power of damping energy. Note that the UP component, which is from a faulty sensor, contains noise only. Damping energy and power plots, normalized by their associated peak values, correspond to band-pass-filtered input signal with corner frequencies: high cut = 20 Hz and low cut = 0.1 Hz. The emergent *P*-phase onset results from $P_{PHASE}P_{ICKER}$ and Akaike Information Criterion (AIC) picker are shown by vertical solid and dashed lines, respectively. The picking results coincide for HNE and HNN components. For the UP component, AIC picker yields a false detection and $P_{PHASE}P_{ICKER}$ returns a null picking, marked as N/A on the plot. The color version of this figure is available only in the electronic edition.

Table 2
Earthquakes Used for Systematic Testing of $P_{PHASE}P_{ICKER}$

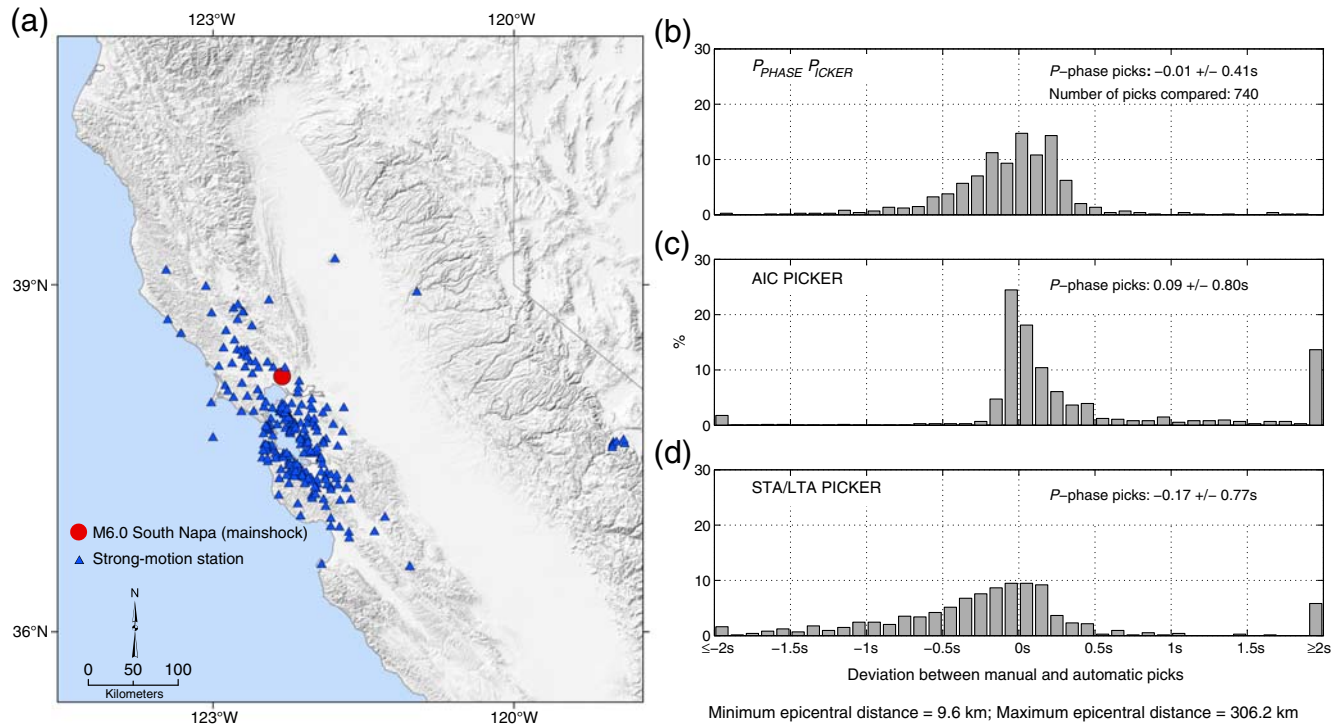| Date (yyyy/mm/dd)	Time (hh:mm:ss.ss)	Latitude (°)	Longitude (°)	Depth (km)	Moment Magnitude	Event ID
2014/08/24	10:20:44.00	38.21517	−122.31233	11.120	6.02	72282711
2014/08/24	12:47:12.55	38.23833	−122.34250	8.439	3.60	72283201

Figure 8. (a) Strong-motion stations within 9.6–306.2 km epicentral distance of the 2014 **M** 6.0 South Napa earthquake. (b, c, and d) The difference between manual and automatic picking times using the $P_{PHASE}P_{ICKER}$, AIC, and short-term-average to long-term-average (STA/LTA) pickers against percentage of three-component strong-motion waveforms. All values beyond 2 (−2) s are compiled at 2 (−2) s. Data correspond to band-pass-filtered acceleration waveforms with corner frequencies: high cut = 20 Hz and low cut = 0.1 Hz. The number of histogram bins used for plotting data in (b), (c), and (d) is 40. The color version of this figure is available only in the electronic edition.

automatic picks are in front of manual picks. There are also many outliers, as indicated by the higher percentage of data populated at −2 and 2 s. Outliers (missed picks, defined as not being within 2 s of the manual pick) are mainly due to noise spikes that were picked by the AIC and/or STA/LTA pickers. The missed picks decreased from 15.1% for the AIC picker and 7.2% for the STA/LTA picker to 0.9% for $P_{PHASE}P_{ICKER}$. Higher SNR values lead to less overall error for all pickers (Fig. 9).

For the weak-motion data set, the Northern California Earthquake Data Center (NCEDC) serves the windowed data and picks for the South Napa earthquake mainshock and aftershocks. These picks were first obtained by an automatic picking algorithm based on the STA/LTA method of Allen (1982) and then manually revised by the USGS analyst. The results are served at NCEDC without making a distinction whether picks are from the automated system or after manual adjustments. Because the benchmark picks were primarily based on the STA/LTA method with revisions, picking results of $P_{PHASE}P_{ICKER}$ are compared only with those from AIC picker. In Figure 10a, the station locations within 3.9–299.9 km that recorded the weak motions of the mainshock are shown. For this data set, the median difference between the automatic and manual picks is 0.01 ± 0.18 s (variance = 0.03 s^2) for $P_{PHASE}P_{ICKER}$ (Fig. 10b), whereas this difference becomes

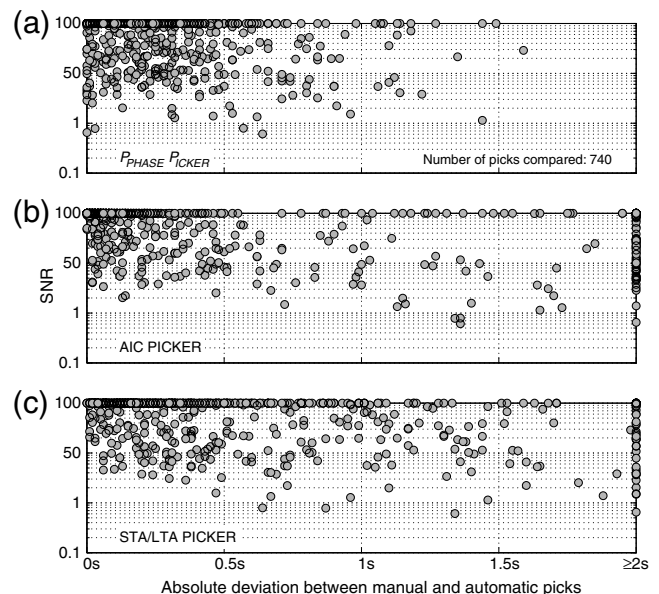**Figure 9.** Absolute difference between manual and automatic picking times using $P_{PHASE}P_{ICKER}$, AIC, and STA/LTA pickers against the SNR values of strong-motion waveforms obtained from the 2014 **M** 6.0 South Napa earthquake. All SNR values beyond 100 are compiled at 100. Data correspond to band-pass-filtered acceleration waveforms with corner frequencies: high cut = 20 Hz and low cut = 0.1 Hz.
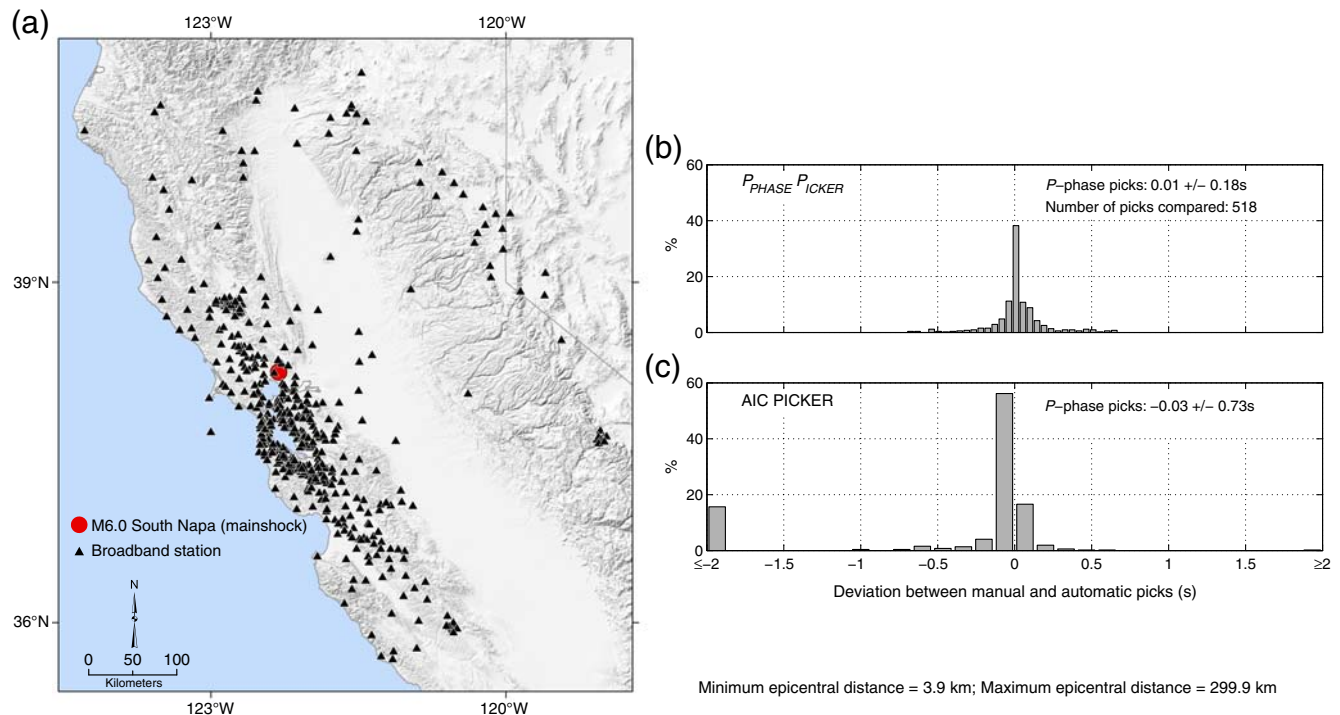
Figure 10. (a) Broadband stations of Northern California Seismic Network within 3.9–299.9 km epicentral distance of the 2014 **M** 6.0 South Napa earthquake. (b and c) The difference between manual and automatic picking times using $P_{PHASE}P_{ICKER}$ and the AIC picker against percentage of weak-motion waveforms. All values beyond 2 (−2) s are compiled at 2 (−2) s. Data correspond to band-pass-filtered velocity waveforms with corner frequencies: high cut = 10 Hz and low cut = 0.5 Hz. The number of histogram bins used for plotting data in (b) and (c) is 30; bin width is smaller in (b) because of smaller variance. The color version of this figure is available only in the electronic edition.
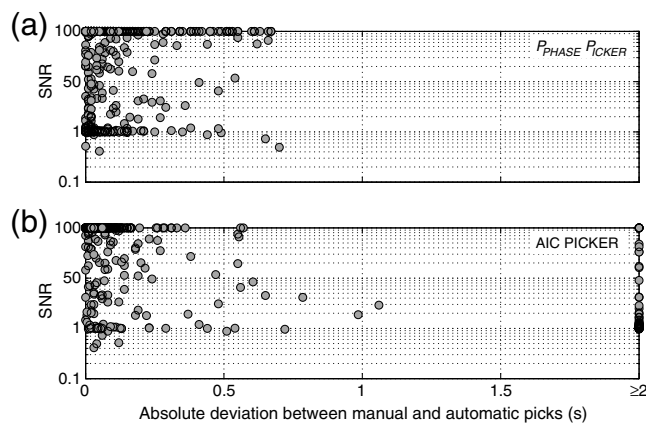
Figure 11. Absolute difference between manual and automatic picking times using $P_{PHASE}P_{ICKER}$ and the AIC picker against the SNR values of weak-motion waveforms obtained from the 2014 **M** 6.0 South Napa earthquake. All SNR values beyond 100 are compiled at 100. Data correspond to band-pass-filtered velocity waveforms with corner frequencies: high cut = 10 Hz and low cut = 0.5 Hz.

-0.03 ± 0.73 s (variance $= 0.54$ s^2) for the AIC picker (Fig. 10c). Similar to the strong-motion data set, the $P_{PHASE}P_{ICKER}$ results are again much closer to benchmark picks; 84% of the compared P-phase picks made by $P_{PHASE}P_{ICKER}$ are less than 0.2 s from the benchmark picks,

compared with 77% using the AIC method. The missed picks decreased from 15.7% for the AIC picker to 0.2% for $P_{PHASE}P_{ICKER}$. Higher SNR values again result in less error for both pickers (Fig. 11).

These findings are further validated with the aftershock velocity data recorded from broadband stations of the Northern California Seismic Network within 2.67–296.4 km epicentral distance (Fig. 12a). For this data set, the median difference between the automatic and manual picks becomes 0.01 ± 0.1 s (variance $= 0.009$ s^2) for $P_{PHASE}P_{ICKER}$ (Fig. 12b), whereas this difference is -0.03 ± 0.6 s (variance $= 0.35$ s^2) for the AIC picker (Fig. 12c). Similar to the mainshock strong- and weak-motion data sets, the $P_{PHASE}P_{ICKER}$ picking results are again much closer to benchmark picks; 93.9% of the compared P-phase picks made by $P_{PHASE}P_{ICKER}$ are less than 0.2 s from the benchmark picks, compared with 73.5% using the AIC method. The missed picks decreased from 6.8% for the AIC picker to 0.76% for $P_{PHASE}P_{ICKER}$. Similar to the observations in Figures 9 and 11, the higher SNR values lead to less overall error for both pickers (Fig. 13).

Conclusions

Automated identification and detection of seismic phases are important for earthquake early warning and rapid processing of large numbers of recordings after major events.
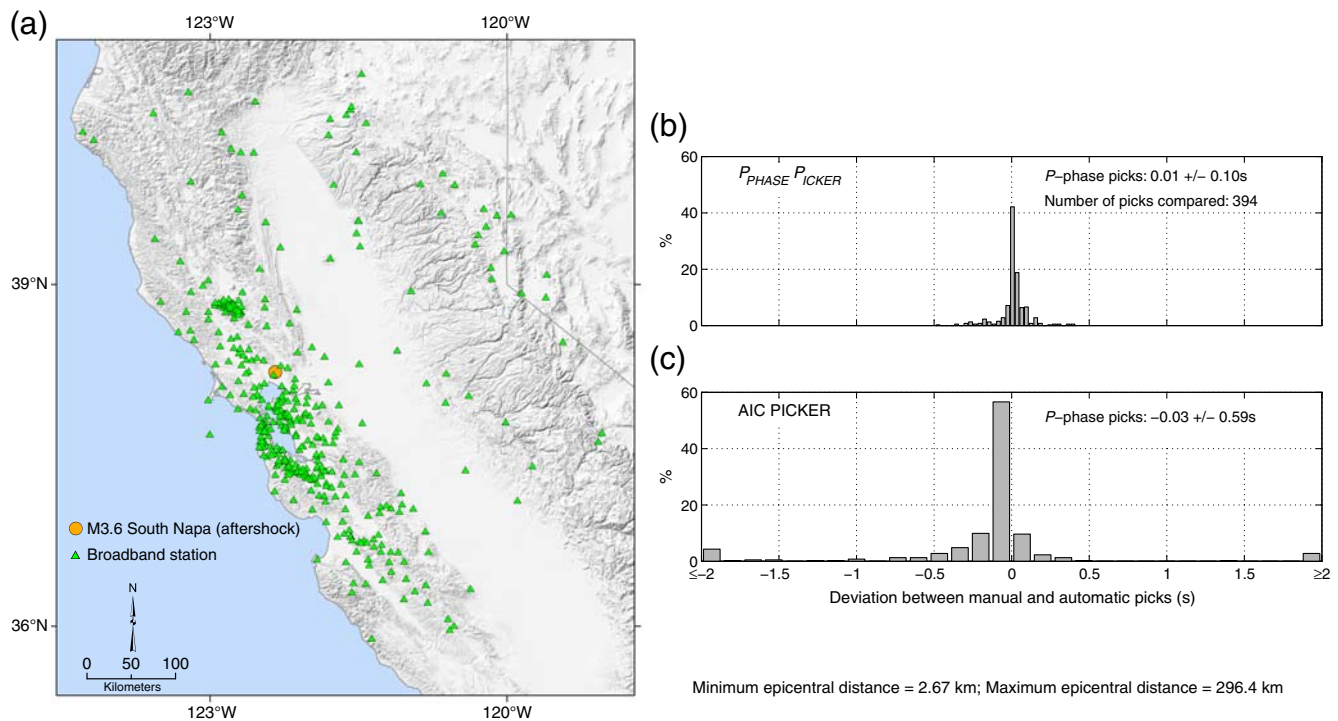
Figure 12. (a) Broadband stations of Northern California Seismic Network within 2.67–296.4 km epicentral distance of the 2014 **M** 3.6 aftershock of the South Napa earthquake. (b and c) The difference between manual and automatic picking times using $P_{PHASE}P_{ICKER}$ and the AIC picker against percentage of weak-motion waveforms. All values beyond 2 (−2) s are compiled at 2 (−2) s. Data correspond to band-pass-filtered velocity waveforms with corner frequencies: high cut = 10 Hz and low cut = 0.5 Hz. The number of histogram bins used for plotting data in (b) and (c) is 30; bin width is smaller in (b) because of smaller variance. The color version of this figure is available only in the electronic edition.
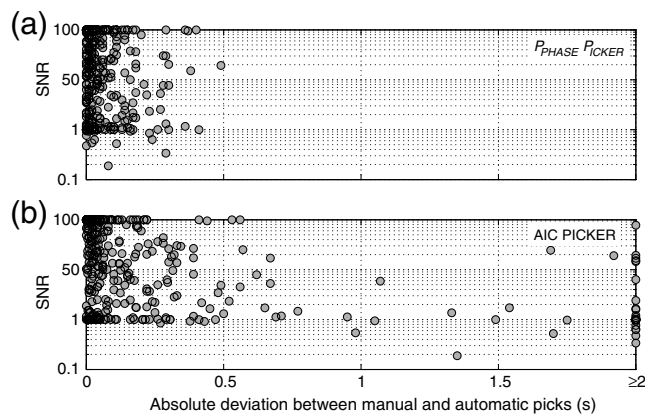
Figure 13. Absolute difference between manual and automatic picking times using $P_{PHASE}P_{ICKER}$ and the AIC picker against the SNR values of weak-motion waveforms obtained from the 2014 **M** 3.6 earthquake (aftershock of the **M** 6.0 South Napa earthquake). All SNR values beyond 100 are compiled at 100. Data correspond to band-pass-filtered velocity waveforms with corner frequencies: high cut = 10 Hz and low cut = 0.5 Hz.

In this article, a new and simple algorithm ($P_{PHASE}P_{ICKER}$) is presented for detecting onset time of the direct P phase in single-component acceleration or broadband velocity records. The algorithm transforms the seismic signal into an SDOF response domain and then uses the damping component of the relative input energy for P-phase picking. The damping energy provides a smooth-envelope function over time, on which the P-phase arrival time can be identified without ambiguity. As compared to conventional picking methods utilizing an STA/LTA, $P_{PHASE}P_{ICKER}$ operates without specifying any detection interval or threshold settings. This means that there is no need for a preparatory study of observation sites or events. $P_{PHASE}P_{ICKER}$ is also amplitude independent, allowing detection of the weak signals' arrival times such as those from microseismic events.

$P_{PHASE}P_{ICKER}$ has been tested by applying it to a series of acceleration and broadband velocity data recorded recently by local networks in northern California, Illinois, Italy, and Thailand. It is demonstrated that the proposed picker is able to accurately detect the onset of genuine signals against the background noise, even in records with a low SNR that was not detectable with a traditional AIC picker. Unlike the AIC picker, $P_{PHASE}P_{ICKER}$ is capable of correctly distinguishing between whether the first arrival is a P-wave (emergent or abrupt) or the signal is from a faulty sensor.

$P_{PHASE}P_{ICKER}$'s performance has been statistically evaluated using 740 strong-motion acceleration waveforms and 518 velocity waveforms from the 2014 **M** 6.0 South Napa earthquake and 394 velocity waveforms from its

M 3.6 aftershock. For the first data set, $P_{PHASE}P_{ICKER}$ picked as many P onsets as the manual picking, with median difference of 0.01 ± 0.41 s. This median difference and standard deviation is less than for the AIC and STA/LTA pickers. The missed picks, defined as not being within 2 s of the manual pick, decreased from 15.1% for the AIC picker and 7.2% for the STA/LTA picker to 0.9% for $P_{PHASE}P_{ICKER}$. The broadband velocity data set yielded similar results. For $P_{PHASE}P_{ICKER}$, the median difference between the automatic and manual picks was 0.01 ± 0.18 s, which is less than that obtained from the AIC picker. The missed picks decreased from 15.7% for the AIC picker to 0.2% for $P_{PHASE}P_{ICKER}$. These test results, including those based on the aftershock data set, collectively indicate that the number and accuracy of the picking are significantly high using $P_{PHASE}P_{ICKER}$.

The picking algorithm described in this article can be a powerful tool for automatically picking P-phase onsets with high precision. $P_{PHASE}P_{ICKER}$ has been integrated into the Automated Processing and Review Interface for Strong Motion Data (PRISM) software of the USGS (Jones *et al.*, 2016) in order to identify the pre-event time window for systematic and automated processing of large numbers of accelerograms. The identification of pre-event duration is important in eliminating background noise and performing effective baseline corrections. $P_{PHASE}P_{ICKER}$ has been tested so far for windowed waveform data; its use for continuous waveform data requires further testing, which is left for future work.

Data and Resources

$P_{PHASE}P_{ICKER}$ is available for MATLAB (www. mathworks.com/products/matlab, last accessed March 2016). Its Ⓔ MATLAB function is provided as the electronic supplement to this article. The 2014 **M** 6.0 South Napa earthquake mainshock and **M** 3.6 aftershock broadband seismic data in mini-SEED format are available at Northern California Earthquake Data Center (http://service.ncedc.org/ncedcws/eventdata/1/, last accessed May 2016) with event IDs 7228271 and 72283201, respectively. The strong-motion acceleration records of these events are available at Center for Engineering Strong-Motion Data (http://www.strongmotioncenter.org/, last accessed March 2016). The strong-motion acceleration record used from the **M** 6.1 earthquake from Thailand is available at Incorporated Research Institutions for Seismology (IRIS) (http://ds.iris.edu/ds/, last accessed March 2016).

Acknowledgments

References

Akaike, H. (1974). A new look at the statistical model identification, *Trans. Automat. Contr.* **19,** no. 6, 716–723, doi: 10.1109/TAC.1974.1100705.

Akazawa, T. (2004). A technique for automatic detection of onset time of P- and S-phases in strong motion records, *Proc. of the 13th World Conference on Earthquake Engineering*, Vancouver, British Columbia, Canada, 1–6 August 2004, Paper Number 786.

Allen, R. V. (1978). Automatic earthquake recognition and timing from single traces, *Bull. Seismol. Soc. Am.* **68,** no. 5, 1521–1532.

Allen, R. V. (1982). Automatic phase pickers: Their present use and future prospects, *Bull. Seismol. Soc. Am.* **72,** no. 6B, 225–242.

Anant, K. S., and F. U. Dowla (1997). Wavelet transform methods for phase identification in three-component seismograms, *Bull. Seismol. Soc. Am.* **87,** no. 6, 1598–1612.

Baer, M., and U. Kradolfer (1987). An automatic phase picker for local and teleseismic events, *Bull. Seismol. Soc. Am.* **77,** no. 4, 1437–1445.

Bai, C. Y., and B. L. N. Kennett (2000). Automatic phase-detection and identification by full use of a single three-component broadband seismogram, *Bull. Seismol. Soc. Am.* **90,** no. 1, 187–198.

Baillard, C., W. C. Crawford, V. Ballu, C. Hibert, and A. Mangeney (2014). An automatic kurtosis-based P- and S-phase picker designed for local seismic networks, *Bull. Seismol. Soc. Am.* **104,** no. 1, doi: 10.1785/0120120347.

Blandford, R. R. (1982). Seismic event discrimination, *Bull. Seismol. Soc. Am.* **72,** 69–87.

Cichowicz, A. (1993). An automatic S-phase picker, *Bull. Seismol. Soc. Am.* **83,** no. 1, 180–189.

Dai, H., and C. MacBeth (1995). Automatic picking of seismic arrivals in local earthquake data using an artificial neural network, *Geophys. J. Int.* **120,** no. 3, 758–774.

Earle, P., and P. Shearer (1994). Characterization of global seismograms using an automatic picking algorithm, *Bull. Seismol. Soc. Am.* **84,** no. 2, 366–376.

Forghani-Arani, F., J. Behura, S. S. Haines, and M. Batzle (2013). An automated cross-correlation based event detection technique and its application to a surface passive data set, *Geophys. Prospect.* **71,** no. 4, 778–787.

Gentili, S., and A. Michelini (2006). Automatic picking of P and S phases using a neural tree, *J. Seismol.* **10,** 39–63.

Hafez, A. G., M. T. A. Khan, and T. Kohda (2010). Clear P-wave arrival of weak events and automatic onset determination using wavelet filter banks, *Digital Signal Process.* **20,** no. 3, 715–723.

Hildyard, M. W., S. E. Nippress, and A. Rietbrock (2008). Event detection and phase picking using a time-domain estimate of predominate period T^{pd}, *Bull. Seismol. Soc. Am.* **98,** 3025–3032.

Institute of Electrical and Electronics Engineers (IEEE) (2003). *Transitions, Pulses, and Related Waveforms*, Vol. 181, IEEE Standard, New York, 54 pp.

Jones, J., E. Kalkan, and C. Stephens (2016). Software for automatic record processing in PRISM, *U.S. Geol. Surv. Open-File Rept.* (in press).

Joswig, M. (1990). Pattern recognition for earthquake detection, *Bull. Seismol. Soc. Am.* **80,** no. 1, 170–186.

Kuperkoch, L., T. Meier, J. Lee, and W. Friederich (2010). Automated determination of P-phase arrival times at regional and local distances using higher order statistics, *Geophys. J. Int.* **181,** no. 1, 1159–1170.

Leonard, M. (2000). Comparison of manual and automatic onset time picking, *Bull. Seismol. Soc. Am.* **90,** no. 6, 1384–1390.

Leonard, M., and B. L. N. Kennett (1999). Multi-component autoregressive techniques for the analysis of seismograms, *Phys. Earth Planet. In.* **113,** 247–263.

Lomax, A., C. Satriano, and M. Vassallo (2012). Automatic picker developments and optimization: FilterPicker—A robust, broadband picker for real-time seismic monitoring and earthquake early warning, *Seismol. Res. Lett.* **83,** no. 3, 531–540.

Maeda, N. (1985). A method for reading and checking phase times in auto-processing system of seismic wave data, *Zisin* **38,** no. 3, 365–379.

Mousset, E., Y. Cansi, R. Crusem, and Y. Souchet (1996). A connectionist approach for automatic labeling of regional seismic phases using a vertical component seismogram, *Geophys. Res. Lett.* **23,** no. 6, 681–684.

Rastin, S. J., C. P. Unsworth, R. Benites, and K. R. Gledhill (2013). Using real and synthetic waveforms of the Matata swarm to assess the performance of New Zealand GeoNet phase pickers, *Bull. Seismol. Soc. Am.* **103,** 2173–2187.

Ross, Z., and Y. Ben-Zion (2014). Automatic picking of direct *P*, *S* seismic phases and fault zone head waves, *Geophys. J. Int.* **199,** 368–381, doi: 10.1093/gji/ggu267.

Ruud, B. O., and E. S. Husebye (1992). A new three-component detector and automatic single-station bulletin production, *Bull. Seismol. Soc. Am.* **82,** 221–237.

Saragiotis, C., L. Hadjileontiadis, and S. Panas (2002). PAI-S/K: A robust automatic seismic *P* phase arrival identification scheme, *IEEE Trans. Geosci. Remote Sens.* **40,** 1395–1404.

Sleeman, R., and T. Van Eck (1999). Robust automatic *P*-phase picking: An on-line implementation in the analysis of broadband seismogram recordings, *Phys. Earth Planet. In.* **113,** 265–275.

Solomon, O. M., D. R. Larson, and N. G. Paulter (2001). Comparison of some algorithms to estimate the low and high state level of pulses, *IEEE Instrumentation and Measurement Technology Conference*, Vol. 1, Budapest, Hungary, 21–23 May 2001, 96–101.

Takanami, T., and G. Kitagawa (1988). A new efficient procedure for the estimation of onset times of seismic waves, *J. Phys. Earth* **36,** 267–290.

Tarvainen, M. (1992). Automatic seismogram analysis: Statistical phase picking and locating methods using one-station three-component data, *Bull. Seismol. Soc. Am.* **82,** 860–869.

Wang, J., and T. L. Teng (1997). Identification and picking of *S* phase using an artificial neural network, *Bull. Seismol. Soc. Am.* **87,** no. 5, 1140–1149.

Zhang, H., C. Thurber, and C. Rowe (2003). Automatic *P*-wave arrival detection and picking with multiscale wavelet analysis for single-component recordings, *Bull. Seismol. Soc. Am.* **93,** no. 5, 1904–1912.

Zhao, Y., and K. Takano (1999). An artificial neural network approach for broadband seismic phase picking, *Bull. Seismol. Soc. Am.* **89,** no. 3, 670–680.

Earthquake Science Center
U.S. Geological Survey
345 Middlefield Road MS 977
Menlo Park, California 94025
ekalkan@usgs.gov